



## RESEARCH ARTICLE

10.1029/2020JD033965

X. Wang and B. Schmidt should be considered joint first author.

### Key Points:

- ECHAM5 global climate simulations for the present day and the mid-Pliocene were dynamically downscaled over the Qaidam Basin (QB)
- Results show a positive imbalance in water balance when the mid-Pliocene climate is imposed on the QB with its modern surface settings
- This imbalance in water balance is closely associated with changes in the midlatitude westerlies and in the East Asian Summer Monsoon

### Supporting Information:

Supporting Information may be found in the online version of this article.

### Correspondence to:

X. Wang and B. Schmidt,  
[xun.wang@tu-berlin.de](mailto:xun.wang@tu-berlin.de);  
[benjamin.schmidt@tu-berlin.de](mailto:benjamin.schmidt@tu-berlin.de)

### Citation:

Wang, X., Schmidt, B., Otto, M., Ehlers, T. A., Mutz, S. G., Botsyun, S., & Scherer, D. (2021). Sensitivity of water balance in the Qaidam Basin to the mid-Pliocene climate. *Journal of Geophysical Research: Atmospheres*, 126, e2020JD033965. <https://doi.org/10.1029/2020JD033965>

Received 25 SEP 2020  
 Accepted 14 JUN 2021

© 2021. The Authors.

This is an open access article under the terms of the [Creative Commons Attribution License](https://creativecommons.org/licenses/by/4.0/), which permits use, distribution and reproduction in any medium, provided the original work is properly cited.

# Sensitivity of Water Balance in the Qaidam Basin to the Mid-Pliocene Climate

Xun Wang<sup>1</sup> , Benjamin Schmidt<sup>1</sup> , Marco Otto<sup>1</sup> , Todd A. Ehlers<sup>2</sup> , Sebastian G. Mutz<sup>2</sup> , Svetlana Botsyun<sup>2</sup> , and Dieter Scherer<sup>1</sup> 

<sup>1</sup>Chair of Climatology, Technische Universität Berlin, Berlin, Germany, <sup>2</sup>Department of Geosciences, University Tübingen, Tübingen, Germany

**Abstract** The Qaidam Basin (QB) in the northeastern Tibetan Plateau held a megalake system during the Pliocene. Today, the lower elevations in the basin are hyperarid. To understand to what extent the climate plays a role in the maintenance of the megalake system during the Pliocene, we applied the Weather Research and Forecasting model for dynamical downscaling of ECHAM5 global climate simulations for the present day and the mid-Pliocene. When imposing the mid-Pliocene climate on the QB with its modern land surface settings, the annual water balance ( $\Delta S$ ), that is, the change in terrestrial water storage within the QB, increases. This positive imbalance of  $\Delta S$  induced solely by the changes in the large-scale climate state would lead to a readjustment of lake extent, until a new equilibrium state is reached, where loss due to evaporation over lake areas compensates for the input by runoff and precipitation. Atmospheric water transport (AWT) analysis at each border of the QB reveals that this imbalance of  $\Delta S$  is caused by stronger moisture influx across the western border in winter, spring, and autumn and weaker moisture out-flux across the eastern border in summer. These changes in AWT are associated with the strengthening of the midlatitude westerlies in all seasons, except for summer, and the intensification of the East Asian Summer Monsoon. Given that the mid-Pliocene climate is an analog to the projected warm climate of the near future, our study contributes to a better understanding of climate change impacts in central Asia.

## 1. Introduction

The Qaidam Basin (QB) is an intermontane endorheic drainage basin located in the northeastern Tibetan Plateau (TP) (Figure 1). The central and lower elevation part of the QB is hyperarid today, but paleogeographic studies revealed that the QB contained a freshwater megalake system during the Pliocene (Chen & Bowler, 1986; Mischke et al., 2010; J. Wang et al., 2012) even though the basin and surrounding mountain areas experienced general aridification throughout the Pliocene (Y. F. Miao et al., 2013; Rieser et al., 2009). With the beginning of the Pleistocene, the megalake system began to shrink. This process continued throughout the Pleistocene until today when only a few playas and saline lakes remain (J. Wang et al., 2012). In the mid-Pliocene (~3 Ma), the global climate was warmer and wetter (Ravelo et al., 2004), while paleogeographic features were similar to those of today (Dowsett et al., 2010). The principal objective of this study is to investigate to what extent climate plays a role in the maintenance of the Qaidam megalake system during the mid-Pliocene.

In an endorheic basin, the steady-state water balance ( $\Delta S$ ) is zero (Broecker, 2010; Ibarra et al., 2018).  $\Delta S$  is defined as the total change in terrestrial water storage (TWS) within all the reservoirs inside the basin. However, changes in climate state can alter the TWS and lead to an imbalanced  $\Delta S$  (e.g., Jiao et al., 2015; Y. Li et al., 2019; J. Wang et al., 2018). A recent study by Scherer (2020) revealed that under the present climate conditions, the  $\Delta S$  in the QB is close to zero, and specific humidity is the main climate driver of the annual  $\Delta S$ . He found that the annual  $\Delta S$  positively correlates with the annual specific humidity. Based on these findings, we hypothesize that a wetter climate state like that of the mid-Pliocene would cause a positive imbalance of the  $\Delta S$  in the QB, which would lead to recharging of groundwater reservoirs and eventually to a rising lake level and an extension of the lake area in the QB. This readjustment of lake extent would continue until a new equilibrium state is reached, where loss due to evaporation over lake areas compensates for the input by runoff and precipitation.

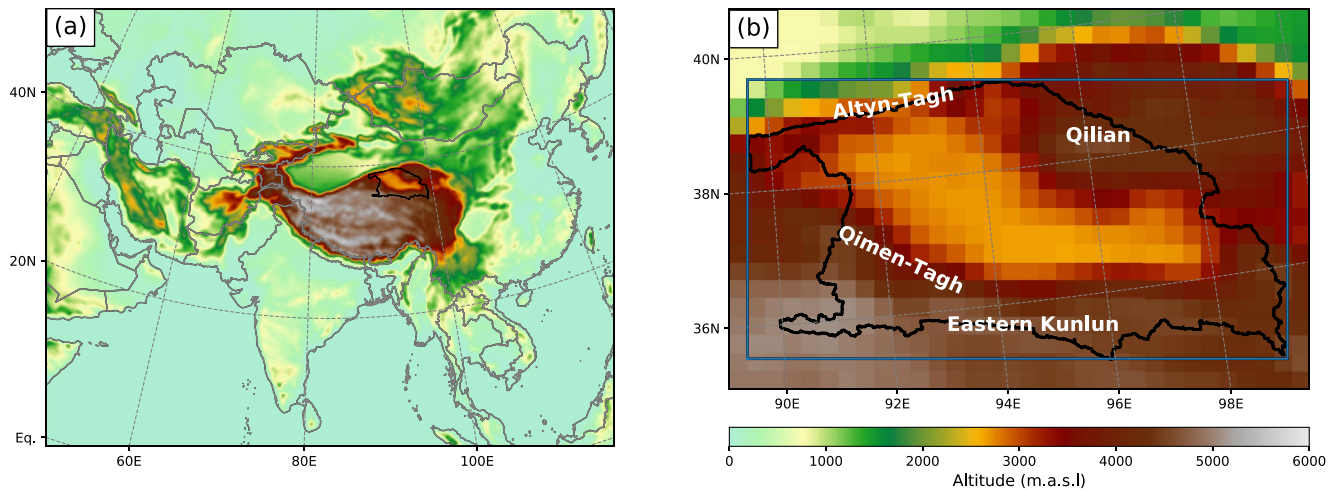


**Figure 1.** (a) Map of Weather Research and Forecasting (WRF) model domain and (b) overview of the Qaidam Basin. Black line: boundary of the Qaidam Basin (Lehner & Grill, 2013). Blue rectangle: Qaidam box for atmospheric moisture budget analysis.

By imposing the mid-Pliocene climate state on the QB with its modern land surface settings (without a megalake system), an imbalance of  $\Delta S$  is induced. From that, we can estimate the lake extent needed to remove this imbalance (hereinafter referred to as the equilibrium lake extent). This can give us an insight into the influence of climate on the existence of the megalake system during the mid-Pliocene. To achieve this, we conducted two regional climate simulations to examine the sensitivity of  $\Delta S$  to changes in large-scale climate state. These two simulations were driven by present-day and mid-Pliocene global climate simulations, respectively. The intention of this study is not to reconstruct the regional climate in the QB during the mid-Pliocene. Instead, we simulated the regional climate of the QB and its surrounding areas with modern surface conditions. In this way, we can analyze the large-scale controls of  $\Delta S$  in the QB independently from other land surface controls.

Scherer (2020) revealed the regional-scale climate driver of the  $\Delta S$ . However, the large-scale controlling mechanisms of  $\Delta S$  in the QB are still not fully understood. On the climatological scale,  $\Delta S$  and net moisture transport into and out of an endorheic basin through its lateral boundary are in balance (Brubaker et al., 1993). Consequently, the changes in  $\Delta S$  in the QB are linked to the changes in atmospheric water transport (AWT). The mid-Pliocene climate is considered as an analog of near-future climates (Burke et al., 2018). Thus, investigating the response of  $\Delta S$  to the mid-Pliocene climate can help us understand the lake development in the future and contribute to water resource management in central Asia.

The goal of this study is to answer the following research questions:

1. How large is the imbalance in  $\Delta S$  in the QB if the mid-Pliocene climate is imposed on the QB with its modern land surface settings? What equilibrium lake extent would be needed to remove this imbalance?
2. How does the AWT differ from the mid-Pliocene climate to the present-day climate?
3. Which large-scale systems regulate the changes in AWT?

The paper is organized as follows: we describe the methods used in this study in the following section. Section 3 presents the dynamical downscaling results for differences in  $\Delta S$ , AWT, and large-scale circulation patterns between the mid-Pliocene and the present climate. Results are discussed and compared with other studies in Section 4. Conclusions are drawn in Section 5.

## 2. Data and Methods

### 2.1. Global Climate Simulations

For the global climate simulations, we used isotope tracking ECHAM5-wiso atmospheric General Circulation Model (GCM), which is developed at Alfred Wegener Institute and based on the ECHAM5 model of the Max Planck Institute for Meteorology, Hamburg (Roeckner et al., 2003). The model is well established

and included in the Coupled Model Intercomparison Projects (Meehl et al., 2007; Taylor et al., 2012). The ability of ECHAM5-wiso to reproduce modern and paleoclimates on both global and regional scales has been shown in multiple studies (Botsyun et al., 2020; Mutz et al., 2016, 2018).

We performed ECHAM5-wiso simulations at a T159 spectral resolution (equivalent to a grid spacing of  $\sim 0.75^\circ$ ) with a vertical resolution of L31 (31 levels up to 10 hPa). The control simulation (PD\_GCM) used present-day boundary conditions including the AMIP2 sea-surface temperature and sea ice data from 1957 to 2014 and observed greenhouse gas concentrations for the same period (Nakicenovic et al., 1990). The simulation was conducted for more than 40 model years. A climatological reference period of 15 years was established for the analysis presented here using the simulation years 2000–2014 to represent the most recent climate conditions. We also performed a paleoclimate experiment, representing the climate conditions of the mid-Pliocene (PLIO\_GCM,  $\sim 3$  Ma). The setups and boundary conditions of PLIO\_GCM for ECHAM5 are identical to those of Mutz et al. (2018) and Botsyun et al. (2020). In PLIO\_GCM, we accounted for changing  $p\text{CO}_2$ , land surface conditions including vegetation change and land ice, albedo, orbital variation, and sea-surface temperatures, which potentially cause changes in the hydrological cycle. The PLIO\_GCM experiment was conducted for 18 years, including 3 years necessary for model spin-up. Both PD\_GCM and PLIO\_GCM experiments were validated against observed and modeled climate patterns (Botsyun et al., 2020; Mutz et al., 2018).

## 2.2. Dynamical Downscaling

We employed Weather Research and Forecasting (WRF) model version 4.1.2 (Skamarock et al., 2019) as the Regional Climate Model for the dynamical downscaling of GCM data. WRF is a fully compressible non-hydrostatic model. Two sensitivity experiments were conducted using 15-year time slices from PD\_GCM and PLIO\_GCM simulated by ECHAM5 (Section 2.1) as initial and boundary conditions. These two WRF experiments are referred to as PD and PLIO in the following text. Except for the atmospheric forcing data, other parameters were kept the same in both experiments (Table 1).

We set the model domain's (Figure 1) grid spacing to 30 km. In the vertical direction, 28 terrain-following eta-levels were used. The model time steps are 120 s with a 6 hourly data output. The boundary conditions were updated every 6 h. We employed the daily reinitialization strategy from Maussion et al. (2011, 2014), where we initialize a model run for every 24 h period. Each simulation starts at 12:00 UTC and contains 36 h, with the first 12 h as the spin-up time. This strategy kept the large-scale circulation patterns simulated by WRF closely constrained by the forcing data, while concurrently allowing WRF to develop the mesoscale atmospheric features. Physical parameterization schemes were consistent with the ones used for high-resolution dynamical downscaling in High Mountain Asia in X. Wang et al. (2021).

To examine the ability of the model to reproduce the present-day climate patterns, PD predicted climate is compared with ERA5 reanalysis data of the European Centre for Medium-Range Weather Forecasts (Copernicus Climate Change Service (C3S), 2017) with regard to precipitation ( $P$ ) and AWT (Figure S1). PD generally reproduces the spatial patterns of  $P$  and AWT. But there exist some discrepancies in the amount of  $P$  and AWT.

## 2.3. Data Analysis

### 2.3.1. Water Balance

In this study,  $\Delta S$  is defined as the total change in TWS within the basin's reservoirs. For endorheic drainage basins like the QB, surface runoff across the basin's border is zero by definition and groundwater runoff can be neglected. The QB has been a closed system at least since the Oligocene (Herb et al., 2015; J. Wang et al., 2012). Thus, the  $\Delta S$  of the QB can be expressed as the spatial average of net precipitation ( $P - ET$ ), that is, the difference between  $P$  and evapotranspiration ( $ET$ ), over the total area of the QB:

$$\Delta S = \langle P - ET \rangle \quad (1)$$

Angle brackets indicate a spatial average over the whole area of the QB (black line in Figure 1b).

**Table 1**  
Basic WRF Model Configurations

<b>Dynamics</b>	
Dynamical solver	Advanced Research WRF (ARW), nonhydrostatic
<b>Maps and grids</b>	
Map projection	Lambert conformal conic
Horizontal grid spacing	30 km (281 × 217 grid points)
Vertical levels	28 Eta-level
<b>Forcing strategy</b>	
Forcing data	ECHAM5 time slices PD_GCM and PLIO_GCM
Lake surface temperature	Substituted by daily mean surface air temperature
Initialization	Daily
Runs starting time	Daily at 12:00 UTC
Runs duration	36 h
Spin-up time	12 h
<b>Physical parameterization schemes</b>	
Longwave radiation	RRTM scheme (Mlawer et al., 1997)
Shortwave radiation	Dudhia scheme (Dudhia, 1989)
Cumulus	Kain-Fritsch cumulus potential scheme (Berg et al., 2013)
Microphysics	Morrison 2-moment scheme (Morrison et al., 2009)
Planetary boundary layer	Yonsei University scheme (Hong et al., 2006)
Land surface model	Unified Noah land surface model (Tewari et al., 2004)
Surface layer	Revised MM5 surface layer scheme (Jiménez et al., 2012)

*Note.* Additional model information can be found in namelists attached in supporting information.

### 2.3.2. Equilibrium Lake Extent Analysis

Several previous studies applied a lake mass balance equation to estimate the equilibrium lake extent (Broecker, 2010; Ibarra et al., 2018). The basic concept is that (a) in the equilibrium state of an endorheic basin, water that feeds the basin's lake (precipitation and runoff from land areas) is in balance with lake evaporation and (b) runoff is generated over land areas, where  $P - ET$  is positive and accumulates in the low-altitude parts of the basin to form or feed lakes:

$$(P_{land} - ET_{land})(A_{QB} - A_{lake}) + P_{lake}A_{lake} = ET_{lake}A_{lake} \quad (2)$$

where  $A$  refers to area and subscripts *land*, *lake*, and *QB* denote corresponding quantities over land, lake, and the whole basin. Rearranging Equation 2 yields:

$$A_{lake} = \frac{P_{land} - ET_{land}}{P_{land} - ET_{land} + ET_{lake} - P_{lake}} A_{QB} \quad (3)$$

Since our PD and PLIO simulations do not contain a lake in the QB, the difference of  $\Delta S$  between PLIO and PD can be considered as the change in  $P_{land} - ET_{land}$ . Thus, by adding the change signal of  $\Delta S$  to the present-day  $P_{land} - ET_{land}$  and assuming constant values of  $E_{lake}$  and  $P_{lake}$ , the equilibrium lake extent that is needed to remove the imbalance in  $\Delta S$  can be estimated.

The present-day  $P_{land} - ET_{land} = 2.4 \text{ mm a}^{-1}$  and  $P_{lake} = 40 \text{ mm a}^{-1}$  are derived from the High Asia Refined (HAR) analysis 10 km products (Maussion et al., 2011, 2014). The HAR is an atmospheric data set generated by dynamical downscaling using WRF. It was comprehensively validated and analyzed (D. Li et al., 2020; Maussion et al., 2014; Pritchard et al., 2019). We calculated three projections with different  $ET_{lake}$ : 600, 800, and 1,000  $\text{mm a}^{-1}$ . These three values represent lower, medium, and upper estimations of lake evaporation

rates over the TP based on previous studies (Haginoya et al., 2009; Lazhu et al., 2016; X. Li et al., 2016; J. Xu et al., 2009; S. Yu et al., 2011).

### 2.3.3. Atmospheric Water Transport

Following Curio et al. (2015), AWT is calculated as the vertical integration of water flux over the whole atmospheric column along the model eta-levels from surface ( $z_{sfc}$ ) to top ( $z_{top}$ ):

$$Q = \int_{z=z_{sfc}}^{z_{top}} v_h \rho q \Delta z \quad (4)$$

where  $v_h$  is the horizontal wind vector,  $\rho$  is the dry air density,  $q$  is the specific humidity for all water species, which is converted from the mixing ratio of water vapor, liquid water, and solid water, and  $\Delta z$  is the thickness of each eta-level, which changes over time and increases with height.

The shape of the QB is very irregular (black line in Figure 1b). A simple rectangle covering the QB (hereafter referred to as Qaidam box) was defined to perform budget analysis on the AWT across the four borders (blue rectangle in Figure 1). This method is widely used to estimate the moisture input and output within a certain area (e.g., Feng & Zhou, 2012; Koffi et al., 2013; Z. Wang et al., 2017). The AWT at each border was calculated and converted to the theoretical precipitation amount. The atmospheric moisture budget of the Qaidam box was then calculated as the sum of the AWT at all borders.

### 2.3.4. Statistical Method

We applied two-sided Welch's  $t$ -tests to assess the uncertainty in the change signal of 15-year means between PD and PLIO. We present  $p$ -values in the form of maps and tables to give a transparent and open assessment of the uncertainty in the change signal without dichotomous treatment of it, following Wasserstein and Lazar (2016). The interpretation of a large number of local hypothesis tests requires a conservative and critical interpretation of the uncertainty of each local test. Thus, the  $p$ -values presented in these maps are adjusted using the false discovery rate adjustment approach by Yekutieli and Benjamini (1999). This method allows a more realistic representation of uncertainty in a field of correlated tests.

## 3. Results

### 3.1. Comparison of $\Delta S$ and its Components

In this section, we focus on the changes in  $\Delta S$  and its components in the High Mountain Asia region and the QB. Figure 2 shows the downscaling results for  $P$ ,  $ET$ , and  $P - ET$  for PLIO and PD and the difference between the two. Maps of adjusted  $p$ -values from two-sided Welch's  $t$ -tests are presented in Figure S2 to show the uncertainty in the change signal of 15-year means between PD and PLIO. Table 2 presents seasonal and annual values of  $P$ ,  $ET$ ,  $\Delta S$ , air temperature at 2 m ( $T_2$ ), and specific humidity at 2 m ( $Q_2$ ) averaged over the QB (black line in Figure 1). The associated  $p$ -values are presented in Table S1.

Over the High Mountain Asia region, simulated  $P$  is enhanced in PLIO over the Himalayas, the northern TP, the Tarim Basin, and the Tien Shan. Lower  $P$  in PLIO can be found in the central TP and Pamir-Karakoram (Figure 2c). In the QB,  $P$  strongly correlates with the altitude for both simulations, due to orographically induced precipitation (Figures 2a and 2b). PLIO generally has higher values of  $P$  in the QB, and the largest difference can be found in the Qilian Mountains, the Altyn-Tagh Mountains, and the Qimen-Tagh ranges. However, the change signal shows large uncertainty on the effect in the Eastern Kunlun Mountains (Figure S2a), which are located in the transition area of positive and negative values of  $P$  difference between PLIO and PD (Figure 2c). Averaged over the whole QB, we see increased  $P$  in all seasons in PLIO with an annual difference between PLIO and PD of  $63 \text{ mm a}^{-1}$  (Table 2).

The spatial patterns of the differences in  $ET$  between PLIO and PD (Figure 2f) generally follow those of the differences in  $P$  (Figure 2c) in large parts of the domain. In these regions, it is not the availability of energy for latent heat, but water availability that limits  $ET$ . We find a different situation in the Pamir-Karakoram region, the northern slopes of the central Himalayas, and the south-eastern part of the QB. This opposite change of  $P$  and  $ET$  in the above-mentioned regions indicates that energy availability must be the limiting factor for  $ET$ . In the QB,  $ET$  mainly takes place in the mountain areas, where most of the precipitation

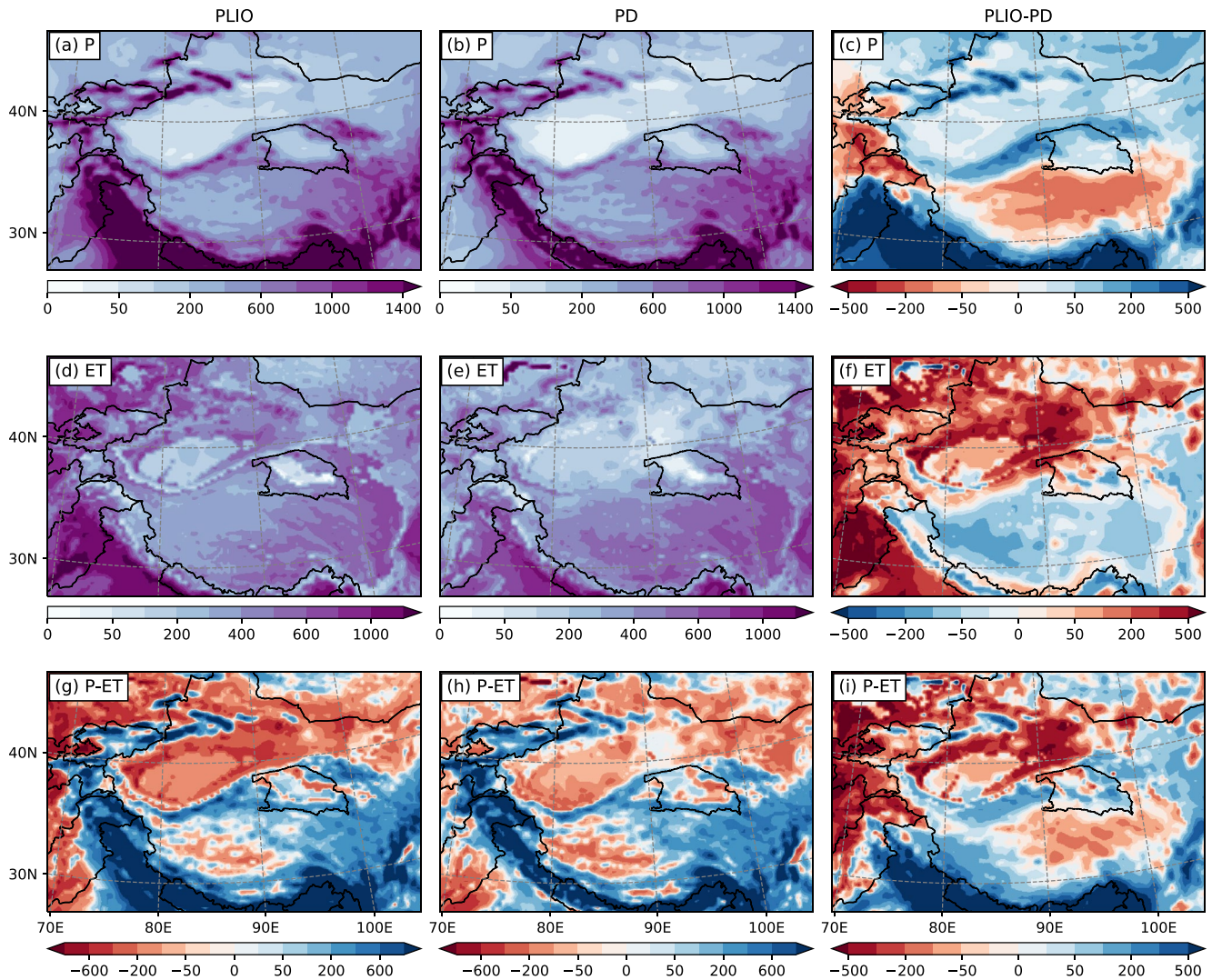


**Figure 2.** Fifteen-year average of annual precipitation  $P$  (a–c), evapotranspiration  $ET$  (d–f), and net precipitation  $P - ET$  (g–i) for PLIO, PD, and difference between PLIO and PD. The unit for all subplots is  $\text{mm a}^{-1}$ .  $p$ -values from two-sided Welch’s  $t$ -test for difference of means between PLIO and PD are presented in Figure S2.

occurs (Figures 2d and 2e). Averaged over the whole QB, PLIO shows an increase in  $ET$  of  $36 \text{ mm a}^{-1}$  compared to PD.

For  $P - ET$ , PLIO and PD yield similar spatial patterns over High Mountain Asia, with negative  $P - ET$  over the western TP, the Tarim Basin, and some parts of the QB (Figures 2g and 2h). In PLIO,  $P - ET$  is decreased over the central TP, the Tarim Basin, and Pamir–Karakoram. The annual  $\Delta S$  in the QB as a whole is  $26 \text{ mm a}^{-1}$  higher in PLIO (Table 2) with a  $p$ -value of 0.058 (Table S1), which is higher than the  $p$ -values of the other quantities. This suggests that the observed effect is real but more research on the topic should be conducted to lower the level of uncertainty. Spatially, a higher  $\Delta S$  in PLIO can be found in the eastern and central parts of the QB (Figure 2i). Seasonally, PLIO has a higher  $\Delta S$  in the QB in winter, spring, and autumn. In summer, the difference in  $\Delta S$  between PLIO and PD is negative (Table 2).

The global climate in the mid-Pliocene is believed to be warmer and wetter than the modern climate, which is also shown in our ECHAM5 global simulations. However, this is not true for the regional climate signal in the QB. While the local  $Q2$  signal averaged over the QB is consistent with the global signal, the local  $T2$  in the QB is 2 K lower in PLIO (Table 2).

**Table 2**

Fifteen-Year Average of Seasonal and Annual Precipitation  $P$  ( $\text{mm Season}^{-1}$  or  $\text{mm a}^{-1}$ ), Evapotranspiration  $ET$  ( $\text{mm Season}^{-1}$  or  $\text{mm a}^{-1}$ ), Water Balance  $\Delta S$  ( $\text{mm Season}^{-1}$  or  $\text{mm a}^{-1}$ ), air Temperature at 2 m  $T_2$  ( $^{\circ}\text{C}$ ), and Specific Humidity at 2 m  $Q_2$  ( $\text{g kg}^{-1}$ ) Averaged Over the Qaidam Basin for PLIO, PD, and the Difference Between PLIO and PD (PLIO – PD)

	PLIO					PD					PLIO – PD				
	$P$	$ET$	$\Delta S$	$T_2$	$Q_2$	$P$	$ET$	$\Delta S$	$T_2$	$Q_2$	$P$	$ET$	$\Delta S$	$T_2$	$Q_2$
DJF	51	22	29	−13.9	1.3	43	25	19	−12.2	1.3	8	−3	11	−1.7	0.0
MAM	131	87	43	−2.7	3.4	111	83	27	0.0	3.1	20	4	17	−2.7	0.3
JJA	163	152	12	8.7	7.4	151	122	29	9.9	6.0	13	30	−17	−1.2	1.4
SON	74	62	12	−3.3	3.3	52	56	−4	−1.0	3.0	22	6	16	−2.3	0.3
Annual	419	322	96	−2.8	3.9	356	286	70	−0.8	3.4	63	36	26	−2.0	0.5

Note.  $p$ -values from two-sided Welch’s  $t$ -tests for difference of means between PLIO and PD can be found in Table S1.

### 3.2. Lake Extent Analysis

In Figure 3, we summarize lake extents ( $A_{\text{lake}}$ ), lake levels ( $z_{\text{lake}}$ ), and the rise in lake levels ( $\Delta z$ ) of three equilibrium lake states under the increase in mean annual  $\Delta S$  of  $26 \text{ mm a}^{-1}$  and three different estimations of  $ET_{\text{lake}}$ . Figure 3 also illustrates these three projected states, where lake extents are estimated using WRF model topography for accumulations of  $P - ET$  and subsequent runoff originating from land in grid points at or below equilibrium lake levels. An increase in mean annual  $\Delta S$  of  $26 \text{ mm a}^{-1}$  would be sufficient to sustain a lake in the QB with an extent ranging from  $7,298$  to  $12,260 \text{ km}^2$ .

### 3.3. Comparison of AWT

Since  $\Delta S$  is linked to the large-scale AWT, in this section, we compare AWT between PLIO and PD. Table 3 presents the seasonal and annual AWT through each border of the Qaidam box (blue rectangle in Figure 1b), as well as the sum of AWT from all borders, that is, the atmospheric moisture budget. In both PLIO and PD, the western and eastern borders of the Qaidam box serve as the dominant moisture input and output channel, respectively. The higher annual moisture budget in PLIO derives from the increased moisture influx across the western border and the decreased moisture export at the eastern border (Table 3). In PLIO, the increased moisture influx at the western border occurs in winter, spring, and autumn, while a strong reduction of moisture export at the eastern border occurs in summer. This indicates that moisture budget and  $\Delta S$  in the QB is related to the large-scale systems that influence the AWT at the western and eastern borders.

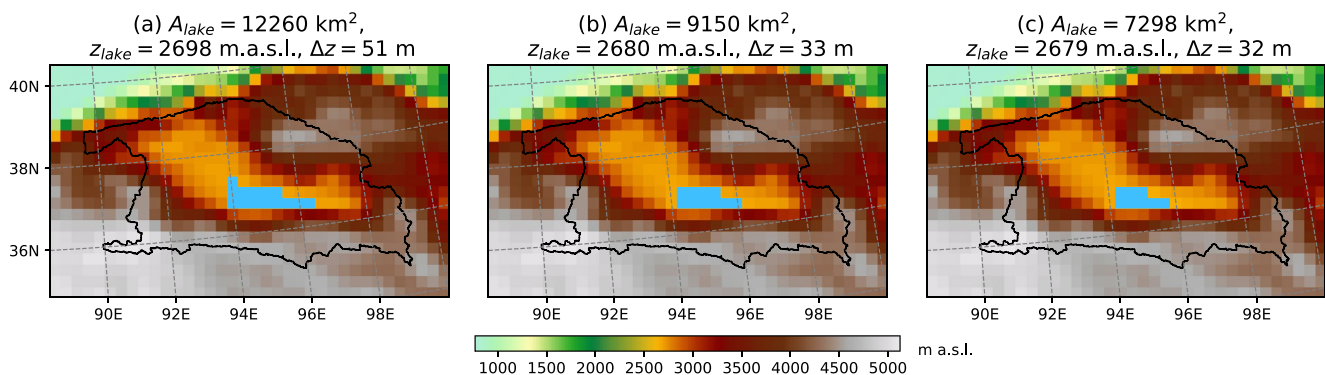


**Figure 3.** Illustrations of simulated lake extents of equilibrium lake states using the present-day model topography from WRF for accumulation of net precipitation in the Qaidam Basin (QB) and subsequent runoff originating from land in areas at or below equilibrium lake levels (marked in blue). The equilibrium lake extent ( $A_{\text{lake}}$ ), lake level ( $z_{\text{lake}}$ ), and the rise in lake level ( $\Delta z$ ) were estimated applying the method described in Section 2.3 using  $26 \text{ mm a}^{-1}$  as input change in mean annual  $\Delta S$  and (a)  $600 \text{ mm a}^{-1}$ , (b)  $800 \text{ mm a}^{-1}$ , and (c)  $1,000 \text{ mm a}^{-1}$  as input lake evaporation ( $E_{\text{lake}}$ ).

**Table 3**

*Fifteen-Year Average of Seasonal and Annual Atmospheric Water Flux Converted to Theoretical Precipitation Amount (mm Season<sup>-1</sup> or mm a<sup>-1</sup>) Through Each Border of the Qaidam Box (Blue Rectangle in Figure 1b)*

	PLIO					PD					PLIO – PD				
	West	East	South	North	Sum	West	East	South	North	Sum	West	East	South	North	Sum
DJF	327	–298	–38	28	19	277	–248	–7	–2	19	50	–50	–31	30	0
MAM	433	–399	50	–49	36	390	–368	19	–14	28	43	–31	31	–35	8
JJA	344	–283	120	–174	8	407	–459	159	–95	12	–63	176	–39	–79	–4
SON	415	–414	71	–79	–7	368	–394	95	–80	–11	47	–20	–24	1	4
Annual	1,519	–1,393	204	–274	56	1,441	–1,469	267	–191	48	78	76	–63	–83	8

*Note.* Positive values indicate moisture input into the Qaidam Basin, while negative values represent moisture output. *p*-values from two-sided Welch's *t*-tests for difference of means between PLIO and PD can be found in Table S2.

Figure 4 illustrates the route and the magnitude of seasonal moisture propagation across the whole domain. In both PD and PLIO, the midlatitude westerlies control the AWT in the QB throughout the year. In winter, spring, and autumn, there exists an eastward moisture transport in the difference plots (Figures 4c, 4f, and 4i), indicating a stronger moisture transport by the midlatitude westerlies in PLIO in these seasons. This is supported by higher moisture input at the western border and higher output at the eastern border in these seasons. In summer months, the influence of the midlatitude westerlies is weaker in PLIO, as shown by the anomalous westward moisture transport over the QB in Figure 4i. Accordingly, the moisture input at the western border and the output at the eastern border are lower in PLIO.

In the summer months, moisture transport is predominantly from the southwest due to the Indian Summer Monsoon (ISM). This northeastward transport over the TP into the QB through the southern border of the Qaidam box is stronger in PD than that in PLIO (Figures 4g–4i and Table 3). Additionally, the moisture transport over eastern Asia by the East Asian Summer Monsoon (EASM) is stronger in PLIO. However, from Figure 4, it is unclear whether the EASM also contributes to the water transport into the QB. Analysis of the daily zonal water transport on the eastern border of the Qaidam box shows moisture input from the eastern border into the QB in PLIO from the middle of July to the beginning of August (Figure 5), which indicates the influence of the EASM in PLIO. This pattern cannot be observed in PD. The additional moisture input by the EASM in PLIO also contributes to the lower values for total moisture output at the eastern border in summer.

### 3.4. Comparison of Large-Scale Circulation Patterns

The results in Section 3.3 show the higher  $\Delta S$  and moisture budget in PLIO are caused by differences in the AWT at the western and eastern borders of the Qaidam box. In this section, we examine the large-scale systems that control the AWT across these two borders.

The AWT at both the western and eastern borders is under the influence of the midlatitude westerlies throughout the year. The seasonal zonal wind speed along a latitude–pressure transect across the longitudinal range of the QB (89°E–100°E) for PLIO and PD is presented in Figure 6. In both PLIO and PD, the midlatitude westerlies show seasonal migrations: a southward extension from summer to winter and a northward contraction from winter to summer. The maximum zonal wind speed occurs at around 200 hPa in all seasons. PLIO shows a poleward shifted and contracted westerly zone. Following the methods used by J. Sun et al. (2020), we defined a strength index as the average maximum zonal wind speed at 200 hPa at each longitude over the Qaidam box to quantify the strength of the westerlies over the QB. Under the mid-Pliocene conditions, the westerlies over the QB are stronger in all seasons except for summer (Figure 7), which explains the larger AWT through the western and eastern borders (Table 3).

Figures 8a–8c show the 500 hPa geopotential height and wind field in summer for PLIO and PD. The Northwest Pacific subtropical high (NPSH) intensifies and extends westwards in PLIO, indicated by higher geopotential and stronger anticyclonic circulation over eastern China (Figure 8a). The NPSH is a major

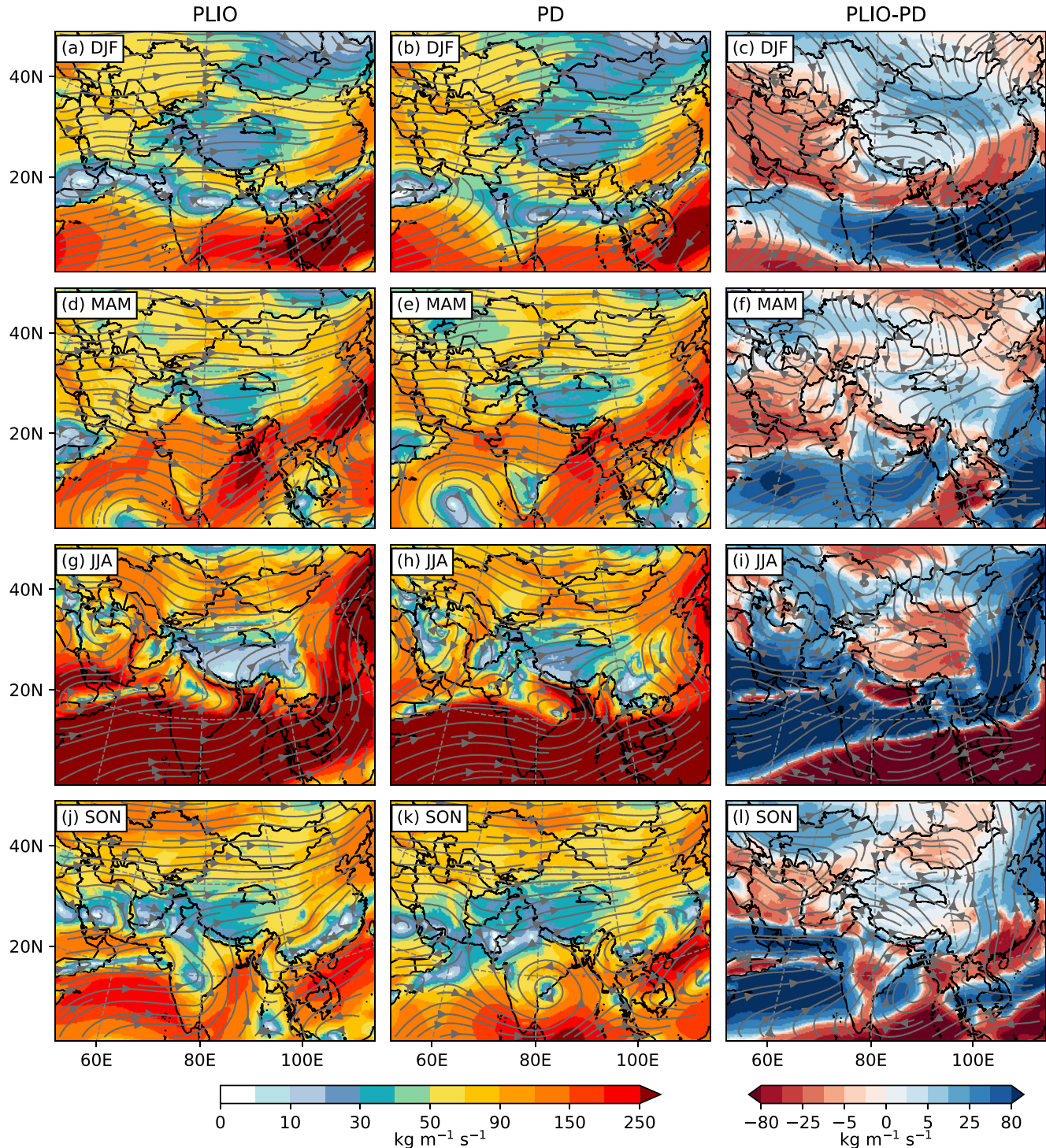


**Figure 4.** Fifteen-year mean seasonal atmospheric water transport ( $\text{kg m}^{-1} \text{s}^{-1}$ ) in DJF (a–c), MAM (d–f), JJA (g–i), and SON (j–l) for PLIO (a, d, g, and j), PD (b, e, h, and k), and the difference between PLIO and PD (c, f, i, and l). Colors represent the strength of water vapor flux; arrows indicate transport direction.

component of the subtropical EASM and regulates the northern edge of the EASM (Huang et al., 2019). The strengthening of the EASM in PLIO is coupled with a tilted jet stream axis over northeastern China. The influence of the EASM on the QB is not visible in the climatology of the summer wind field at the 500 hPa level. Therefore, we selected the period from July 17 to July 27, when the daily AWT averaged over all the grid points at the eastern border of the Qaidam box is negative (westward), to define the period, when the

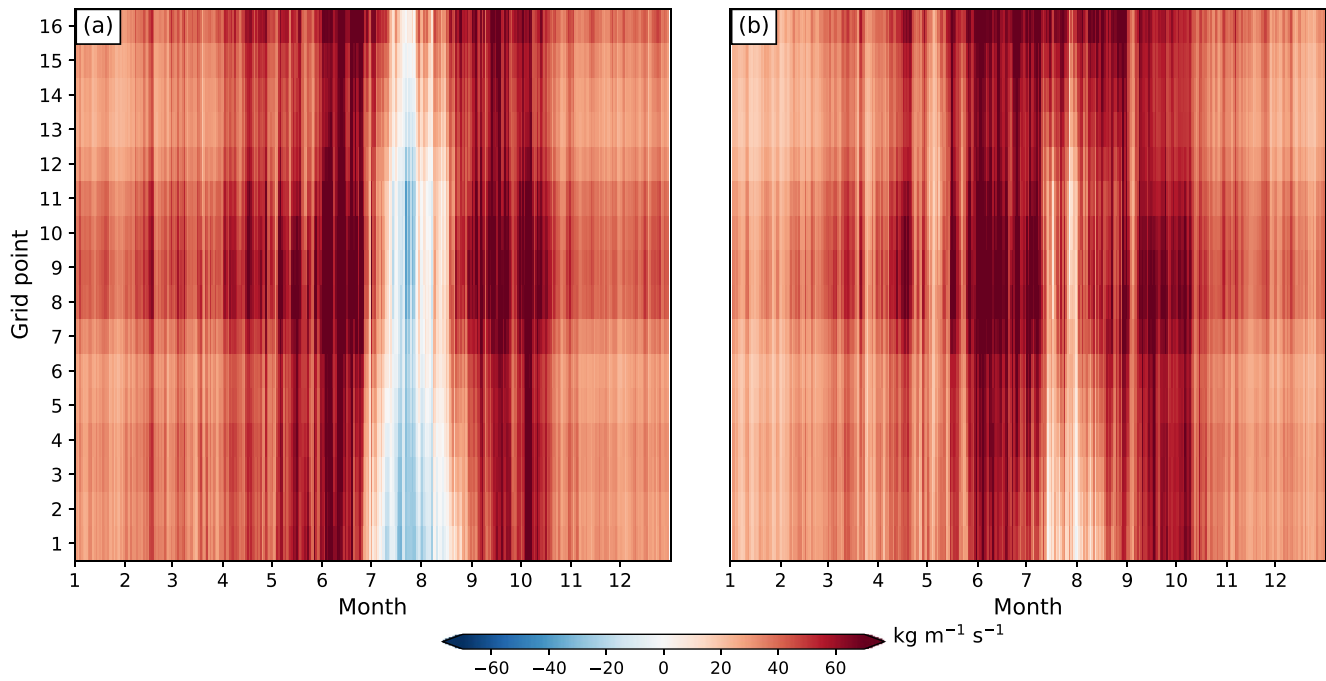


**Figure 5.** Fifteen-year average of daily zonal atmospheric water transport ( $\text{kg m}^{-1} \text{s}^{-1}$ ) of 16 grid points at the eastern border of the Qaidam box (blue rectangle in Figure 1b) for (a) PLIO and (b) PD. Grid point 1 and grid point 16 represent the south-most and north-most grid point. Reddish colors indicate water transport away from the Qaidam Basin, while blueish colors indicate water transport toward the Qaidam Basin.

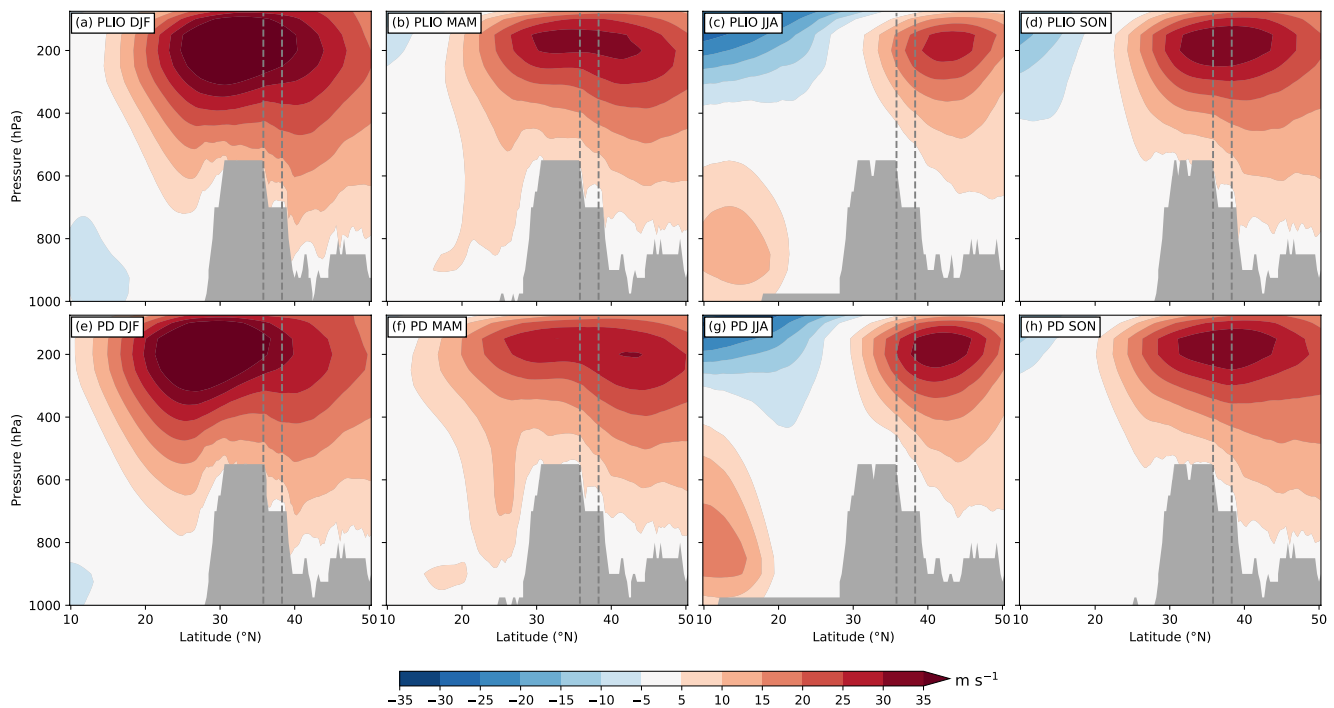


**Figure 6.** Fifteen-year average of seasonal zonal wind speed ( $\text{m s}^{-1}$ ) along a latitude–pressure transect averaged from  $89^{\circ}\text{E}$ – $100^{\circ}\text{E}$  for PLIO (a–d) and PD (e–h) in DJF (a and e), MAM (b and f), JJA (c and g), and SON (d and h). Dashed lines show the latitudinal range of the Qaidam Basin.

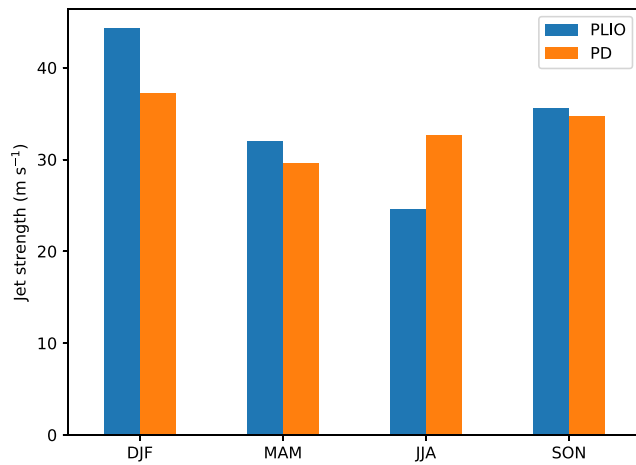


**Figure 7.** Fifteen-year average of seasonal strength index of jet stream ( $\text{m s}^{-1}$ ) over the Qaidam Basin for PLIO and PD, calculated as defined in J. Sun et al. (2020).

QB is under the direct influence of the EASM. The geopotential height and wind field at 500 hPa in this period are presented in Figures 8d–8f. During this period, the NPSH intensifies and extends further northwestward in both PLIO and PD, as compared to the climatology in the summer. In PLIO, the southern part of the QB is clearly under the control of easterly winds in this period (Figure 8d).

## 4. Discussion

### 4.1. Implications of the Higher $\Delta S$ in the QB in PLIO

The PLIO simulation presented here cannot be considered as a reconstruction of the regional climate in the QB for the mid-Pliocene. A reconstruction is neither the intention of this study nor is possible at this time at a grid spacing of 30 km. This would require Pliocene surface conditions, such as topography and land cover, at an equivalent or even higher resolution, which are not available to date. The most commonly used surface boundary conditions for mid-Pliocene simulations are from the US Geological Survey's Pliocene Research Interpretation and Synoptic Mapping (PRISM) project (Dowsett et al., 1994). The most recently released PRISM4 data set has a  $1^\circ \times 1^\circ$  grid spacing (Dowsett et al., 2016), which is too coarse for regional climate simulations at a grid spacing of 30 km. Moreover, the exact extent and location of the Qaidam megalake system in the mid-Pliocene is unknown. We took only required meteorological fields from the ECHAM5 model to drive the WRF model and applied the same geographical static data from WRF Preprocessing System for both PLIO and PD simulations. This approach has the benefit of isolating the influence of atmospheric variables on the hydroclimate of the QB from other factors, such as land cover and vegetation changes.

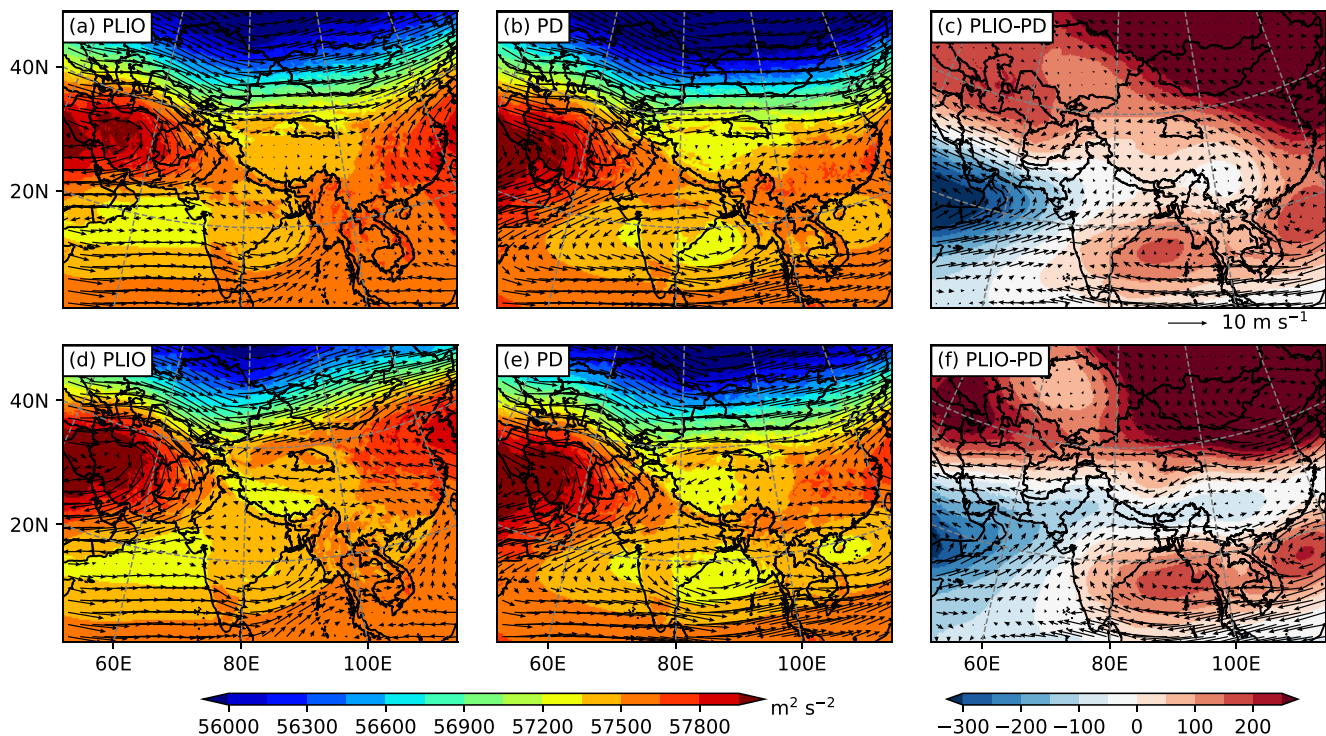


**Figure 8.** Fifteen-year climatology of geopotential (shading,  $\text{m}^2 \text{s}^{-2}$ ) and wind field (arrows,  $\text{m s}^{-1}$ ) at 500 hPa averaged in JJA (a–c) and from July 17 to July 27 (d–f) for PLIO, PD, and PLIO – PD.

Therefore, the PLIO simulation cannot be interpreted on its own but in conjunction with the PD simulation. Interpretation of the simulation results should focus on the differences between PLIO and PD simulations. The QB has a higher  $\Delta S$  in PLIO than in PD. This imbalance in  $\Delta S$  induced solely by the changes in large-scale atmospheric circulations could result in a lake much larger than Lake Qinghai, the largest salt lake in China (4,317 km<sup>2</sup>), as shown in our lake extent analysis (Section 3.2). The maximum lake extent of 59,000 km<sup>2</sup> approximated from proxy data (Chen & Bowler, 1986) is still much larger than the estimations we present here. This indicates that factors besides large-scale atmospheric circulation also contributed to sustaining the megalake system during the Pliocene.

#### 4.2. Comparison With Pliocene Model Intercomparison Project Simulations

The changes in large-scale circulation patterns in PLIO are in good agreement with recent modeling studies (Huang et al., 2019; X. Li et al., 2015; Zhang et al., 2013). The results of these studies are based on simulations in the Pliocene Model Intercomparison Project (PlioMIP) using PRISM3D as boundary conditions, which is the same as our forcing ECHAM5 simulation for the mid-Pliocene. X. Li et al. (2015) found a global poleward shift of the midlatitude westerlies and an increase of zonal wind on the poleward flank of the westerly jet in the mid-Pliocene. The poleward shift of the midlatitude westerlies is accompanied by a poleward shift of Hadley and Ferrel cells. The intensification and northwestward extension of the EASM in the mid-Pliocene are also simulated by models in PlioMIP (Huang et al., 2019; Zhang et al., 2013). Huang et al. (2019) compared modeled results to paleontological data from 43 sites throughout China. The northern margin of the EASM indicated by the wet–dry boundary located further northwest in the mid-Pliocene (Figure 4 in Huang et al. [2019]), which is roughly consistent with their modeled results.

In addition, we compared PD and PLIO simulations, and PD\_GCM and PLIO\_GCM simulations generated by ECHAM5 with COSMOS (Stepanek & Lohmann, 2012) and HadCM3 (Bragg et al., 2012) simulations, in terms of  $P$ . These two are the end-members of PlioMIP in simulated, regionally averaged annual precipitation deviations from the preindustrial, as identified by Zhang et al. (2013). As shown in Figure 9, the coarse end-members COSMOS and HadCM3 are not able to produce orographic precipitation patterns correctly, such as those along the Himalayan orogen. Our high-resolution ECHAM5 simulations already show improvements. Nevertheless, the skill of GCMs in predicting orographic precipitation remains limited (e.g., Meehl et al., 2007). This is particularly true at the scale of interest in this study. At coarse grid resolutions, orography is systematically lower than at fine grid resolutions, such that blocking of air masses and orographically induced precipitation are generally underestimated. While the latter effect generally leads to an underestimation of total precipitation, less blocking could act in both directions. Less blocking could result in excessive AWT, which does not necessarily lead to more precipitation since for this atmospheric water to become precipitable, a trigger is needed (Lin et al., 2018). Consequently, the direction in which less blocking changes precipitation remains complicated. In addition, the WRF runs use a nonhydrostatic pressure solver while GCMs assume hydrostatic conditions, which further improves predictions of relatively small-scale phenomena that departures from the hydrostatic balance (Yang et al., 2017). In total, the WRF dynamical downscaling is able to physically resolve mesoscale atmospheric processes that are not included in GCM simulations. Given the aforementioned differences between WRF and GCMs, it is therefore not surprising that mean annual mid-Pliocene precipitation deviation simulated with WRF shows some discrepancies to GCM (Figure 10). Although the big picture of precipitation deviations from WRF is in line with ECHAM5, disagreement can be found over the complex terrains on the TP. WRF exhibits possible improvements, for example, in the eastern Himalayas and over the TP, where the spatial patterns of precipitation deviations are more coherent than in ECHAM5.

#### 4.3. Large-Scale Systems Controlling the $\Delta S$ in the QB

There exists a debate on which large-scale system dominates the hydroclimate in the QB in previous studies based on proxy reconstructions. Caves et al. (2015) summarized published data of the spatial distribution of oxygen isotopes in precipitation over High Mountain Asia since the early Eocene (~56 Ma BP). They found that sites at the QB show consistently higher  $\delta O_{18}$  values in the paleo-precipitation than sites in the southern TP, which indicates that westerlies have dominated the moisture supply over the QB since the early Eocene. The authors concluded that the reduction in moisture supply by the westerlies since the early Eocene,

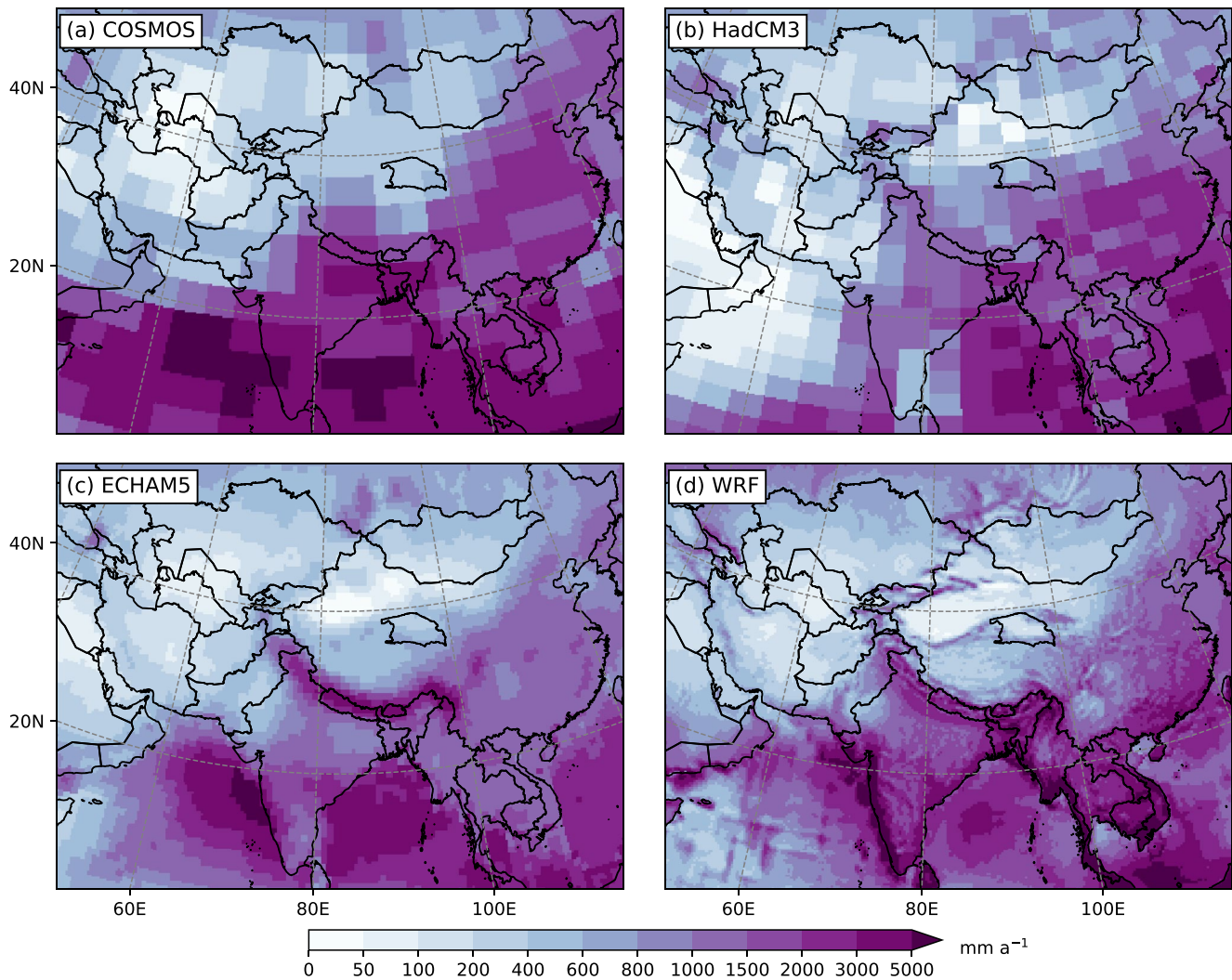


**Figure 9.** Mean annual mid-Pliocene precipitation climatologies for Pliocene Model Intercomparison Project (PlioMIP) simulations conducted with (a) COSMOS and (b) HadCM3, and for this study's simulations conducted with (c) ECHAM5 and (d) WRF.

rather than uplift of the TP or changes in ISM strength, is the driver of the step-wise drying in central Asia. The modern EASM is believed to have a weak or no influence on the QB (e.g., Huang et al., 2019; L. Yu & Lai, 2012). This is also shown in our PD simulation. There is no westward moisture transport across the eastern border of the Qaidam box in the course of the year (Figure 5b). G. Xu et al. (2011) found correlation between the tree ring  $\delta O_{18}$  series collected from the eastern margin of the QB and the strength of EASM from 1873 to 1975. Y. Miao et al. (2011) examined a pollen record from the KC-1 core, which was extracted in the western part of the QB and covers a period of 18–5 Ma. A transition from a warm-wet climate to a cold-dry climate was found in the QB during this period, and the authors concluded that this transition was driven by the evolution of the East Asian Monsoon system. Our moisture budget analysis shows that the midlatitude westerlies dominate the AWT over the QB in both PLIO and PD (Table 3). However, the difference in the moisture budget in the QB between PLIO and PD is a combined effect of changes in the midlatitude westerlies and the EASM.

#### 4.4. Implications for the Future

The mid-Pliocene warm period is a potential analog of future anthropogenic warming since both periods feature a higher  $CO_2$  concentration than the modern level (Burke et al., 2018). Previous studies reveal that both the mid-Pliocene and projected future climates show similar large-scale atmospheric circulations to

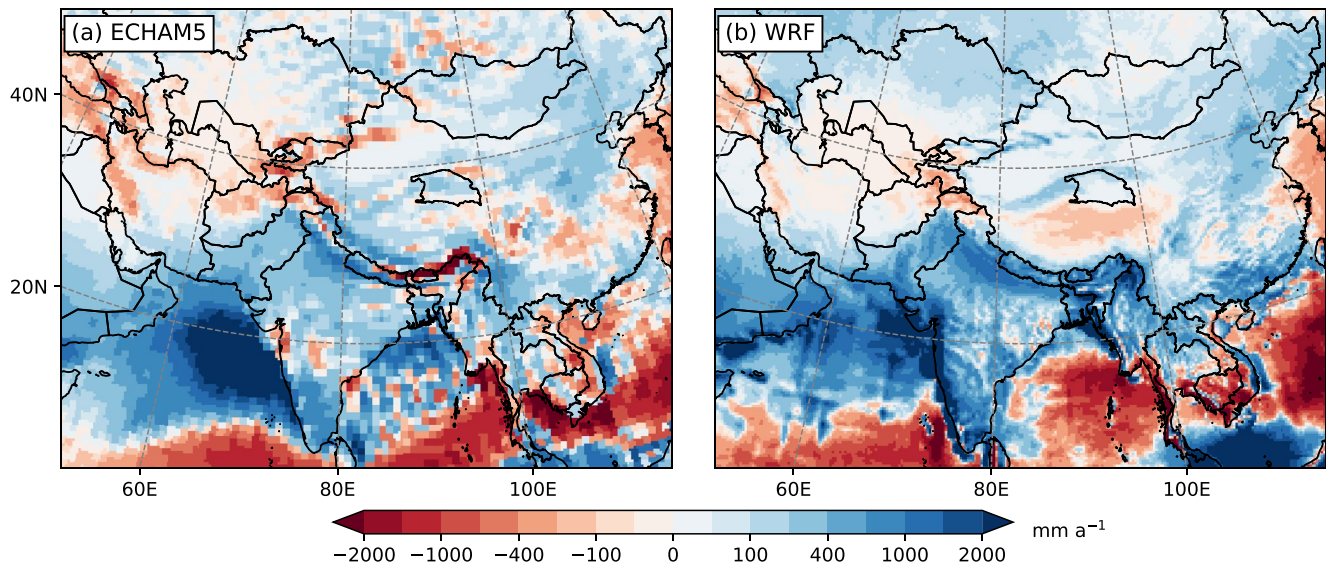


**Figure 10.** Mean annual mid-Pliocene precipitation deviations for (a) ECHAM5 and (b) WRF from present-day precipitation.

some extent. For example, Y. Sun et al. (2013) applied three Atmosphere–Ocean GCM simulations for Representative Concentration Pathway (RCP) 4.5 scenario, mid-Pliocene, and present day. Their results showed a poleward expansion and an intensification of the Hadley cell over the subtropics under both mid-Pliocene and future climates, but the response of the Walker cell depicts some discrepancies. A conclusion was drawn that the Hadley cell in the mid-Pliocene can be a good analog of the Hadley cell in the future due to the linear relationship between the south–north thermal contrast and the CO<sub>2</sub> concentration. But this analog hypothesis has limitations since the response of the east–west thermal contrast to CO<sub>2</sub> concentration is more complicated and not similar. The monsoon dynamics between the mid-Pliocene climate and the projected future climate under the Extended Concentration Pathway version 4.5, which is an extension of RCP4.5 beyond 2100, were also investigated in a prior study (Y. Sun et al., 2018), who found that both climates show large-scale similarities and an enhanced EASM, which is due to the increase in thermally controlled large-scale moisture transport.

Combined with our results and discussions, the high similarity of large-scale circulations between the mid-Pliocene climate and the projected future climate implies a possible transient state in the QB, during which  $\Delta S$  will increase, if the EASM extends into the QB and AWT by the westerlies increases. The increased  $\Delta S$  would lead to the recharge of groundwater reservoirs and subsequent rise of lake levels in the QB until  $\Delta S$  is balanced again.

## 5. Conclusions

In this study, we utilized the WRF model for dynamical downscaling of ECHAM5 global simulations for the present day and the mid-Pliocene. The downscaling results show that when imposing the mid-Pliocene climate to the QB with its modern land surface settings, the annual  $\Delta S$  would increase by 26 mm a<sup>-1</sup>. This positive imbalance of  $\Delta S$  induced only by the changes in the large-scale climate state would be sufficient to sustain a lake in the QB with an extent ranging from 7,298 to 12,260 km<sup>2</sup>, depending on the value of  $ET_{\text{lake}}$ .

The annual moisture budget in the QB is higher in PLIO, corresponding with the higher  $\Delta S$ . Higher moisture input from the western border and lower moisture output at the eastern border are the main reasons for the higher annual moisture budget and higher  $\Delta S$  in PLIO. These two borders are both under the influence of midlatitude westerlies. The eastern border is additionally regulated by the EASM in PLIO. In PLIO, the midlatitude westerlies contract poleward and intensify over the QB in winter, spring, and autumn, transporting more moisture into the QB through its western border. In summer, the strengthening of the EASM accompanied by weakened westerlies in PLIO leads to the decrease of moisture output at the eastern border.

We conclude that the strengthening of the midlatitude westerlies in all seasons, except for summer, and the intensification of the EASM lead to higher moisture budget and higher  $\Delta S$  in the QB in PLIO.

The mid-Pliocene climate shares similarities in large-scale circulations with projected future climate scenarios. Thus, our results can contribute to a better understanding of the impacts of climate change and future lake development in central Asia. Our results also highlight the added values of applying high-resolution GCM and dynamical downscaling by WRF. High resolution can resolve fundamental processes over complex terrains, such as orographic precipitation and AWT, more realistically.

### Data Availability Statement

The WRF V4.1.2 model used in this study is freely available under the official website of WRF: <http://dx.doi.org/10.5065/D6MK6B4K>. The setup files for the WRF model are included in the supporting information. The WRF model output data used in this study are available at [https://doi.org/10.26050/WDC/RRA\\_WRF\\_simulations](https://doi.org/10.26050/WDC/RRA_WRF_simulations).

### Acknowledgments

This work was supported by the German Federal Ministry of Education and Research (BMBF) program “Central Asia – Monsoon Dynamics and Geo-Ecosystems II” (CAME II) within Q-TIP project “Quaternary Tipping Points of Lake Systems in the Arid Zone of Central Asia” (code 03G08063C and 03G08063A to D. Scherer and to T. A. Ehlers, respectively). The authors thank Tom Grassmann for his administrative work on the high-performance computing cluster. This open-access publication was funded by Technische Universität Berlin.

### References

- Berg, L. K., Gustafson, W. I., Kassianov, E. I., & Deng, L. (2013). Evaluation of a modified scheme for shallow convection: Implementation of cup and case studies. *Monthly Weather Review*, *141*(1), 134–147. <https://doi.org/10.1175/mwr-d-12-00136.1>
- Botsyun, S., Ehlers, T., Mutz, S., Methner, K., Krstnik, E., & Mulch, A. (2020). Opportunities and challenges for paleoaltimetry in “small” orogens: Insights from the European Alps. *Geophysical Research Letters*, *47*, e2019GL086046. <https://doi.org/10.1029/2019GL086046>
- Bragg, F., Lunt, D. J., & Haywood, A. (2012). Mid-Pliocene climate modelled using the UK Hadley Centre Model: PlioMIP Experiments 1 and 2. *Geoscientific Model Development*, *5*(5), 1109–1125. <https://doi.org/10.5194/gmd-5-1109-2012>
- Broecker, W. (2010). Long-term water prospects in the western United States. *Journal of Climate*, *23*(24), 6669–6683. <https://doi.org/10.1175/2010jcli3780.1>
- Brubaker, K. L., Entekhabi, D., & Eagleson, P. (1993). Estimation of continental precipitation recycling. *Journal of Climate*, *6*(6), 1077–1089. [https://doi.org/10.1175/1520-0442\(1993\)006<1077:eocpr>2.0.co;2](https://doi.org/10.1175/1520-0442(1993)006<1077:eocpr>2.0.co;2)
- Burke, K. D., Williams, J. W., Chandler, M. A., Haywood, A. M., Lunt, D. J., & Otto-Bliesner, B. L. (2018). Pliocene and Eocene provide best analogs for near-future climates. *Proceedings of the National Academy of Sciences of the United States of America*, *115*(52), 13288–13293. <https://doi.org/10.1073/pnas.1809600115>
- Caves, J. K., Winnick, M. J., Graham, S. A., Sjöström, D. J., Mulch, A., & Chamberlain, C. P. (2015). Role of the westerlies in central Asia climate over the Cenozoic. *Earth and Planetary Science Letters*, *428*, 33–43. <https://doi.org/10.1016/j.epsl.2015.07.023>
- Chen, K., & Bowler, J. M. (1986). Late Pleistocene evolution of salt lakes in the Qaidam Basin, Qinghai Province, China. *Palaeogeography, Palaeoclimatology, Palaeoecology*, *54*(1–4), 87–104.
- Copernicus Climate Change Service (C3S). (2017). *ERA5: Fifth generation of ECMWF atmospheric reanalyses of the global climate*. Copernicus Climate Change Service Climate Data Store (CDS). Retrieved from <https://cds.climate.copernicus.eu/cdsapp#!/home>
- Curio, J., Maussion, F., & Scherer, D. (2015). A 12-year high-resolution climatology of atmospheric water transport over the Tibetan Plateau. *Earth System Dynamics*, *6*(1), 109–124. <https://doi.org/10.5194/esd-6-109-2015>
- Dowsett, H., Dolan, A., Rowley, D., Moucha, R., Forte, A. M., Mitrovica, J. X., et al. (2016). The PRISM4 (mid-Piacenzian) paleoenvironmental reconstruction. *Climate of the Past*, *12*(7), 1519–1538. <https://doi.org/10.5194/cp-12-1519-2016>
- Dowsett, H., Robinson, M., Haywood, A., Salzmann, U., Hill, D., Sohl, L., et al. (2010). The PRISM3D paleoenvironmental reconstruction. *Stratigraphy*, *7*(2–3), 123–139.
- Dowsett, H., Thompson, R., Barron, J., Cronin, T., Fleming, F., Ishman, S., et al. (1994). Joint investigations of the middle Pliocene climate I: Prispaleoenvironmental reconstructions. *Global and Planetary Change*, *9*(3–4), 169–195. [https://doi.org/10.1016/0921-8181\(94\)90015-9](https://doi.org/10.1016/0921-8181(94)90015-9)
- Dudhia, J. (1989). Numerical study of convection observed during the winter monsoon experiment using a mesoscale two-dimensional model. *Journal of the Atmospheric Sciences*, *46*(20), 3077–3107. [https://doi.org/10.1175/1520-0469\(1989\)046<3077:nsocod>2.0.co;2](https://doi.org/10.1175/1520-0469(1989)046<3077:nsocod>2.0.co;2)
- Feng, L., & Zhou, T. (2012). Water vapor transport for summer precipitation over the Tibetan Plateau: Multidata set analysis. *Journal of Geophysical Research*, *117*, D20114. <https://doi.org/10.1029/2011JD017012>
- Haginoya, S., Fujii, H., Kuwagata, T., Xu, J., Ishigooka, Y., Kang, S., & Zhang, Y. (2009). Air–lake interaction features found in heat and water exchanges over Nam Co on the Tibetan Plateau. *Sola*, *5*, 172–175. <https://doi.org/10.2151/sola.2009-044>
- Herb, C., Koutsodendris, A., Zhang, W., Appel, E., Fang, X., Voigt, S., & Pross, J. (2015). Late Plio-Pleistocene humidity fluctuations in the western Qaidam Basin (NE Tibetan Plateau) revealed by an integrated magnetic-palynological record from lacustrine sediments. *Quaternary Research (United States)*, *84*(3), 457–466. <https://doi.org/10.1016/j.yqres.2015.09.009>
- Hong, S.-Y., Noh, Y., & Dudhia, J. (2006). A new vertical diffusion package with an explicit treatment of entrainment processes. *Monthly Weather Review*, *134*(9), 2318–2341. <https://doi.org/10.1175/mwr3199.1>
- Huang, X., Jiang, D., Dong, X., Yang, S., Su, B., Li, X., et al. (2019). Northwestward migration of the northern edge of the East Asian summer monsoon during the mid-Pliocene warm period: Simulations and reconstructions. *Journal of Geophysical Research: Atmospheres*, *124*, 1392–1404. <https://doi.org/10.1029/2018JD028995>
- Ibarra, D. E., Oster, J. L., Winnick, M. J., Caves Rugenstein, J. K., Byrne, M. P., & Chamberlain, C. P. (2018). Warm and cold wet states in the western United States during the Pliocene–Pleistocene. *Geology*, *46*(4), 355–358. <https://doi.org/10.1130/g39962.1>
- Jiao, J. J., Zhang, X., Liu, Y., & Kuang, X. (2015). Increased water storage in the Qaidam Basin, the North Tibet Plateau from grace gravity data. *PLoS One*, *10*(10), e0141442. <https://doi.org/10.1371/journal.pone.0141442>
- Jiménez, P. A., Dudhia, J., González-Rouco, J. F., Navarro, J., Montávez, J. P., & García-Bustamante, E. (2012). A revised scheme for the WRF surface layer formulation. *Monthly Weather Review*, *140*(3), 898–918. <https://doi.org/10.1175/mwr-d-11-00056.1>
- Koffi, E., Graham, E., & Mätzler, C. (2013). The water vapour flux above Switzerland and its role in the August 2005 extreme precipitation and flooding. *Meteorologische Zeitschrift*, *22*(3), 328–341. <https://doi.org/10.1127/0941-2948/2013/0392>

- Lazhu, Yang, K., Wang, J., Lei, J., Chen, Y., Zhu, Y., et al. (2016). Quantifying evaporation and its decadal change for Lake Nam Co, central Tibetan Plateau. *Journal of Geophysical Research: Atmospheres*, *121*, 7578–7591. <https://doi.org/10.1002/2015JD024523>
- Lehner, B., & Grill, G. (2013). Global river hydrography and network routing: Baseline data and new approaches to study the world's large river systems. *Hydrological Processes*, *27*(15), 2171–2186. <https://doi.org/10.1002/hyp.9740>
- Li, D., Yang, K., Tang, W., Li, X., Zhou, X., & Guo, D. (2020). Characterizing precipitation in high altitudes of the western Tibetan Plateau with a focus on major glacier areas. *International Journal of Climatology*, *40*(12), 5114–5127. <https://doi.org/10.1002/joc.6509>
- Li, X., Jiang, D., Zhang, Z., Zhang, R., Tian, Z., & Yan, Q. (2015). Mid-Pliocene westerlies from PlioMIP simulations. *Advances in Atmospheric Sciences*, *32*(7), 909–923. <https://doi.org/10.1007/s00376-014-4171-7>
- Li, X., Ma, Y., Huang, Y., Hu, X., Wu, X., Wang, P., et al. (2016). Evaporation and surface energy budget over the largest high-altitude saline lake on the Qinghai–Tibet Plateau. *Journal of Geophysical Research: Atmospheres*, *121*, 10–470. <https://doi.org/10.1002/2016JD025027>
- Li, Y., Su, F., Chen, D., & Tang, Q. (2019). Atmospheric water transport to the endorheic Tibetan Plateau and its effect on the hydrological status in the region. *Journal of Geophysical Research: Atmospheres*, *124*, 12864–12881. <https://doi.org/10.1029/2019JD031297>
- Lin, C., Chen, D., Yang, K., & Ou, T. (2018). Impact of model resolution on simulating the water vapor transport through the central Himalayas: Implication for models' wet bias over the Tibetan Plateau. *Climate Dynamics*, *51*(9–10), 3195–3207. <https://doi.org/10.1007/s00382-018-4074-x>
- Maussion, F., Scherer, D., Finkelnburg, R., Richters, J., Yang, W., & Yao, T. (2011). WRF simulation of a precipitation event over the Tibetan Plateau, China—An assessment using remote sensing and ground observations. *Hydrology and Earth System Sciences*, *15*(6), 1795–1817. <https://doi.org/10.5194/hess-15-1795-2011>
- Maussion, F., Scherer, D., Mölg, T., Collier, E., Curio, J., & Finkelnburg, R. (2014). Precipitation seasonality and variability over the Tibetan Plateau as resolved by the High Asia reanalysis. *Journal of Climate*, *27*(5), 1910–1927. <https://doi.org/10.1175/jcli-d-13-00282.1>
- Meehl, G. A., Covey, C., Delworth, T., Latif, M., McAvaney, B., Mitchell, J. F. B., et al. (2007). The WCRP CMIP3 multimodel dataset: A new era in climate change research. *Bulletin of the American Meteorological Society*, *88*(9), 1383–1394. <https://doi.org/10.1175/bams-88-9-1383>
- Miao, Y., Fang, X., Herrmann, M., Wu, F., Zhang, Y., & Liu, D. (2011). Miocene pollen record of KC-1 core in the Qaidam Basin, NE Tibetan Plateau and implications for evolution of the East Asian monsoon. *Palaeogeography, Palaeoclimatology, Palaeoecology*, *299*(1–2), 30–38. <https://doi.org/10.1016/j.palaeo.2010.10.026>
- Miao, Y. F., Fang, X. M., Wu, F. L., Cai, M. T., Song, C. H., Meng, Q. Q., & Xu, L. (2013). Late Cenozoic continuous aridification in the western Qaidam Basin: Evidence from sporopollen records. *Climate of the Past*, *9*(4), 1863–1877. <https://doi.org/10.5194/cp-9-1863-2013>
- Mischke, S., Sun, Z., Herzschuh, U., Qiao, Z., & Sun, N. (2010). An ostracod-inferred large Middle Pleistocene freshwater lake in the presently hyper-arid Qaidam Basin (NW China). *Quaternary International*, *218*(1–2), 74–85. <https://doi.org/10.1016/j.quaint.2009.03.002>
- Mlawer, E. J., Taubman, S. J., Brown, P. D., Iacono, M. J., & Clough, S. A. (1997). Radiative transfer for inhomogeneous atmospheres: RRTM, a validated correlated-k model for the longwave. *Journal of Geophysical Research*, *102*(D14), 16663–16682. <https://doi.org/10.1029/97jd00237>
- Morrison, H., Thompson, G., & Tatarskii, V. (2009). Impact of cloud microphysics on the development of trailing stratiform precipitation in a simulated squall line: Comparison of one- and two-moment schemes. *Monthly Weather Review*, *137*(3), 991–1007. <https://doi.org/10.1175/2008mwr2556.1>
- Mutz, S. G., Ehlers, T. A., Li, J., Steger, C., Paeth, H., Werner, M., & Poulos, C. J. (2016). Precipitation  $\delta^{18}\text{O}$  over the Himalaya-Tibet orogen from ECHAM5-iso simulations: Statistical analysis of temperature, topography and precipitation. *Journal of Geophysical Research: Atmospheres*, *121*, 9278–9300. <https://doi.org/10.1002/2016JD024856>
- Mutz, S. G., Ehlers, T. A., Werner, M., Lohmann, G., Stepanek, C., & Li, J. (2018). Estimates of late Cenozoic climate change relevant to Earth surface processes in tectonically active orogens. *Earth Surface Dynamics*, *6*(2), 271–301. <https://doi.org/10.5194/esurf-6-271-2018>
- Nakicenovic, N., Alcamo, J., Davis, G., De Vries, B., Fenhann, J., Gaffin, S., et al. (1990). *Special report on emissions scenarios: A special report of Working Group III of the Intergovernmental Panel on Climate Change* (Technical Report).
- Pritchard, D. M., Forsythe, N., Fowler, H. J., O'Donnell, G. M., & Li, X.-F. (2019). Evaluation of Upper Indus near-surface climate representation by WRF in the High Asia Refined analysis. *Journal of Hydrometeorology*, *20*(3), 467–487.
- Ravelo, A. C., Andreasen, D. H., Lyle, M., Lyle, A. O., & Wara, M. W. (2004). Regional climate shifts caused by gradual global cooling in the Pliocene epoch. *Nature*, *429*(6989), 263–267.
- Rieser, A. B., Bojar, A.-V., Neubauer, F., Genser, J., Liu, Y., Ge, X.-H., & Friedl, G. (2009). Monitoring Cenozoic climate evolution of northeastern Tibet: Stable isotope constraints from the western Qaidam Basin, China. *International Journal of Earth Sciences*, *98*(5), 1063–1075.
- Roeckner, E., Baeuml, G., Bonaventura, L., Brokopf, R., Esch, M., Giorgetta, M., et al. (2003). *The General Circulation Model ECHAM5. Part I: Model description* (Technical Report).
- Scherer, D. (2020). Survival of the Qaidam mega-lake system under mid-Pliocene climates and its restoration under future climates. *Hydrology and Earth System Sciences*, *24*(7), 3835–3850. <https://doi.org/10.5194/hess-24-3835-2020>
- Skamarock, W., Klemp, J., Dudhia, J., Gill, D., Zhiquan, L., Berner, J., et al. (2019). *A description of the advanced research WRF model version 4 NCAR technical note* (Technical Report). NCAR-UCAR. Retrieved from <http://library.ucar.edu/research/publish-technote>
- Stepanek, C., & Lohmann, G. (2012). Modeling mid-Pliocene climate with cosmos. *Geoscientific Model Development*, *5*, 1221–1243. <https://doi.org/10.5194/gmd-5-1221-2012>
- Sun, J., Yang, K., Guo, W., Wang, Y., He, J., & Lu, H. (2020). Why has the inner Tibetan Plateau become wetter since the mid-1990s? *Journal of Climate*, *33*, 8507–8522.
- Sun, Y., Ramstein, G., Contoux, C., & Zhou, T. (2013). A comparative study of large-scale atmospheric circulation in the context of a future scenario (RCP4.5) and past warmth (mid-Pliocene). *Climate of the Past*, *9*(4), 1613–1627. <https://doi.org/10.5194/cp-9-1613-2013>
- Sun, Y., Ramstein, G., Li, L. Z., Contoux, C., Tan, N., & Zhou, T. (2018). Quantifying East Asian summer monsoon dynamics in the ECP4.5 scenario with reference to the mid-Piacenzian warm period. *Geophysical Research Letters*, *45*, 12523–12533. <https://doi.org/10.1029/2018GL080061>
- Taylor, K. E., Stouffer, R. J., & Meehl, G. A. (2012). An overview of CMIP5 and the experiment design. *Bulletin of the American Meteorological Society*, *93*(4), 485–498. <https://doi.org/10.1175/bams-d-11-00094.1>
- Tewari, M., Chen, F., Wang, W., Dudhia, J., LeMone, M., Mitchell, K., et al. (2004). Implementation and verification of the unified Noah land surface model in the WRF model. In *Paper presented at 20th Conference on Weather Analysis and Forecasting/16th Conference on Numerical Weather Prediction* (Vol. 1115, pp. 2165–2170).
- Wang, J., Fang, X., Appel, E., & Song, C. (2012). Pliocene–Pleistocene climate change at the NE Tibetan Plateau deduced from lithofacies variation in the drill core SG-1, western Qaidam Basin, China. *Journal of Sedimentary Research*, *82*(12), 933–952.

- Wang, J., Song, C., Reager, J. T., Yao, F., Famiglietti, J. S., Sheng, Y., et al. (2018). Recent global decline in endorheic basin water storages. *Nature Geoscience*, *11*(12), 926–932. <https://doi.org/10.1038/s41561-018-0265-7>
- Wang, X., Tolksdorf, V., Otto, M., & Scherer, D. (2021). WRF-based dynamical downscaling of ERA5 reanalysis data for High Mountain Asia: Toward a new version of the High Asia Refined analysis. *International Journal of Climatology*, *41*(1), 743–762. <https://doi.org/10.1002/joc.6686>
- Wang, Z., Duan, A., Yang, S., & Ullah, K. (2017). Atmospheric moisture budget and its regulation on the variability of summer precipitation over the Tibetan Plateau. *Journal of Geophysical Research: Atmospheres*, *122*, 614–630. <https://doi.org/10.1002/2016JD025515>
- Wasserstein, R. L., & Lazar, N. A. (2016). *The ASA statement on p-values: Context, process, and purpose*. Taylor & Francis.
- Xu, G., Chen, T., Liu, X., An, W., Wang, W., & Yun, H. (2011). Potential linkages between the moisture variability in the northeastern Qaidam Basin, China, since 1800 and the East Asian summer monsoon as reflected by tree ring  $\delta^{18}\text{O}$ . *Journal of Geophysical Research*, *116*, D09111. <https://doi.org/10.1029/2010JD015053>
- Xu, J., Yu, S., Liu, J., Haginoya, S., Ishigooka, Y., Kuwagata, T., et al. (2009). The implication of heat and water balance changes in a lake basin on the Tibetan Plateau. *Hydrological Research Letters*, *3*, 1–5. <https://doi.org/10.3178/hrl.3.1>
- Yang, Q., Leung, L. R., Lu, J., Lin, Y.-L., Hagos, S., Sakaguchi, K., & Gao, Y. (2017). Exploring the effects of a nonhydrostatic dynamical core in high-resolution aquaplanet simulations. *Journal of Geophysical Research: Atmospheres*, *122*, 3245–3265. <https://doi.org/10.1002/2016JD025287>
- Yekutieli, D., & Benjamini, Y. (1999). Resampling-based false discovery rate controlling multiple test procedures for correlated test statistics. *Journal of Statistical Planning and Inference*, *82*(1), 171–196. [https://doi.org/10.1016/s0378-3758\(99\)00041-5](https://doi.org/10.1016/s0378-3758(99)00041-5)
- Yu, L., & Lai, Z. (2012). OSL chronology and palaeoclimatic implications of aeolian sediments in the eastern Qaidam Basin of the northeastern Qinghai–Tibetan Plateau. *Palaeogeography, Palaeoclimatology, Palaeoecology*, *337*, 120–129. <https://doi.org/10.1016/j.palaeo.2012.04.004>
- Yu, S., Liu, J., Xu, J., & Wang, H. (2011). Evaporation and energy balance estimates over a large inland lake in the Tibet–Himalaya. *Environmental Earth Sciences*, *64*(4), 1169–1176. <https://doi.org/10.1007/s12665-011-0933-z>
- Zhang, R., Yan, Q., Zhang, Z. S., Jiang, D., Otto-Bliesner, B. L., Haywood, A. M., et al. (2013). Mid-Pliocene East Asian monsoon climate simulated in the PlioMIP. *Climate of the Past*, *9*, 2085–2099. <https://doi.org/10.5194/cp-9-2085-2013>